Chemical Science

ROYAL SOCIETY OF CHEMISTRY

EDGE ARTICLE

View Article Online
View Journal | View Issue

Cite this: *Chem. Sci.*, 2023, **14**, 14290

All publication charges for this article have been paid for by the Royal Society of Chemistry

A near-infrared light-activated nanoprobe for simultaneous detection of hydrogen polysulfide and sulfur dioxide in myocardial ischemia–reperfusion injury†

Xianzhu Luo, Cuiling Zhang,* Chenyang Yue, Yuelin Jiang, Fei Yang and Yuezhong Xian*

Ischemia–reperfusion-induced cardiomyocyte mortality constitutes a prominent contributor to global morbidity and mortality. However, early diagnosis and preventive treatment of cardiac I/R injury remains a challenge. Given the close relationship between ferroptosis and I/R injury, monitoring their pathological processes holds promise for advancing early diagnosis and treatment of the disease. Herein, we report a near-infrared (NIR) light-activated dual-responsive nanoprobe (UCNP@mSiO$_2$@SP-NP-NAP) for controllable detection of hydrogen polysulfide (H_2S_n) and sulfur dioxide (SO_2) during ferroptosis-related myocardial I/R injury. The nanoprobe's responsive sites could be activated by NIR and Vis light modulation, reversibly alternating for at least 5 cycles. We employed the nanoprobe to monitor the fluctuation levels of H_2S_n and SO_2 in H9C2 cardiomyocytes and mice, revealing that H_2S_n and SO_2 levels were up-regulated during I/R. The NIR light-activated dual-responsive nanoprobe could be a powerful tool for myocardial I/R injury diagnosis. Moreover, we also found that inhibiting the initiation of the ferroptosis process contributed to attenuating cardiac I/R injury, which indicated great potential for treating I/R injury.

Received 19th September 2023
Accepted 23rd November 2023

DOI: 10.1039/d3sc04937j

rsc.li/chemical-science

Introduction

Ischemic heart disease is the leading cause of widespread mortality worldwide, with millions dying from the disease every year.[1] Currently, reperfusion is the mainstay of treatment for acute ischemic heart disease.[2,3] However, the myocardial ischemia–reperfusion (I/R) process can cause severe damage to the myocardium due to oxidative stress and inflammatory responses.[4] Therefore, early diagnosis and preventive treatment of I/R disease is essential. Ferroptosis is a non-apoptotic form of cell death introduced by the Stockwell group in 2012.[5] Noteworthily, recent studies have shown that ferroptosis is inextricably linked to cardiac I/R injury, but the mechanism of action is unclear.[6,7] Thus, understanding the relationship between ferroptosis and I/R may provide new strategies to reduce I/R injury.

Ferroptosis occurs primarily through the inhibition of the cystine/glutamate transporter protein (system Xc^-) or reduced activity of glutathione peroxidase 4 (GPX4).[5–7] Sulfur dioxide (SO_2) and hydrogen polysulfides (H_2S_n), as metabolites of cysteine (Cys) and glutathione (GSH), are closely related to the occurrence of ferroptosis.[8–10] However, their mechanisms of action have rarely been studied. Moreover, hydrogen sulfide (H_2S) has been widely studied as one of the three major gaseous signaling molecules over the last few decades, and recent studies have suggested that H_2S_n is also a key regulator of cell signalling.[11–13] Previous studies have shown that hydropersulfides and persulfides play critical roles in protecting the heart from I/R injury and anthracycline-induced cardiotoxicity.[14–17] It is essential to monitor the level of H_2S_n in cardiac I/R, given that hydropersulfides and persulfides undergo metabolism to H_2S_n *in vivo*.[18] In addition, SO_2 is considered the fourth gaseous signaling molecule, which exhibits an integral role in the effective regulation of vasodilation and blood pressure, as well as an antioxidant.[19–21] Therefore, there is a need to develop sensitive methods to gain insight into the important role of H_2S_n and SO_2 in the signaling of ferroptosis. However, it is still challenging to controllably detect dual-signaling molecules for SO_2 and H_2S_n.

In contrast to conventional fluorescent probes, light-activated fluorescent probes can be conveniently regulated by exposing specific reaction sites to light.[22,23] This capability offers great potential for accurate disease diagnosis.[24,25] Furthermore, employing light to modulate the responsiveness of fluorescent probes represents a minimally invasive approach for achieving

Shanghai Engineering Research Center of Molecular Therapeutics and New Drug Development, Department of Chemistry, School of Chemistry and Molecular Engineering, East China Normal University, Shanghai 200241, China. E-mail: clzhang@chem.ecnu.edu.cn; yzxian@chem.ecnu.edu.cn

† Electronic supplementary information (ESI) available. See DOI: https://doi.org/10.1039/d3sc04937j

high spatiotemporal resolution in bioimaging.[26–28] Yin's group developed a UV-activated probe for precise detection of SO_2 in heat shock cells and tissues.[26] Weissleder's group exploited a series of UV-light-deactivated rhodamine derivatives for highly multiplexed and cyclic fluorescence imaging in cells.[29] Nevertheless, weak tissue penetration and high phototoxicity of UV light limit their potential in biological systems.[30–32] Near-infrared (NIR) light, known for its deep tissue penetration and minimal photodamage, is particularly suited for bioimaging.[33–35] Notably, lanthanide-doped upconversion nanoparticles (UCNPs) can convert the NIR excitation into UV emission, commonly employed as a photo-control element.[36,37] Compared with single-function fluorescent probes, multi-response probes can perform multiple tasks simultaneously, and they show unique advantages in the diagnosis of diseases with multiple pieces of molecular information.[38,39]

Motivated by the above challenges, we rationally designed a NIR light-activated dual-responsive fluorescent nanoprobe for the detection and bioimaging of H_2S_n and SO_2 in a cardiac I/R injury model. This nanoprobe was developed by encapsulating the light-activated dye (SP-NP-NAP) within mesoporous silica-coated upconversion nanoparticles (UCNP@mSiO$_2$@SP-NP-NAP) (Scheme 1 and S1†). Notably, the nanoprobe was not activated without NIR light stimulation, ensuring precise determination of H_2S_n and SO_2 in the specific cells or tissue locations. Upon NIR light exposure, the masked dual-responsive sites of SP-NP-NAP could be triggered *in situ*, enabling controlled monitoring of H_2S_n and SO_2. And the nanoprobe monitored the dynamic fluctuation of H_2S_n and SO_2

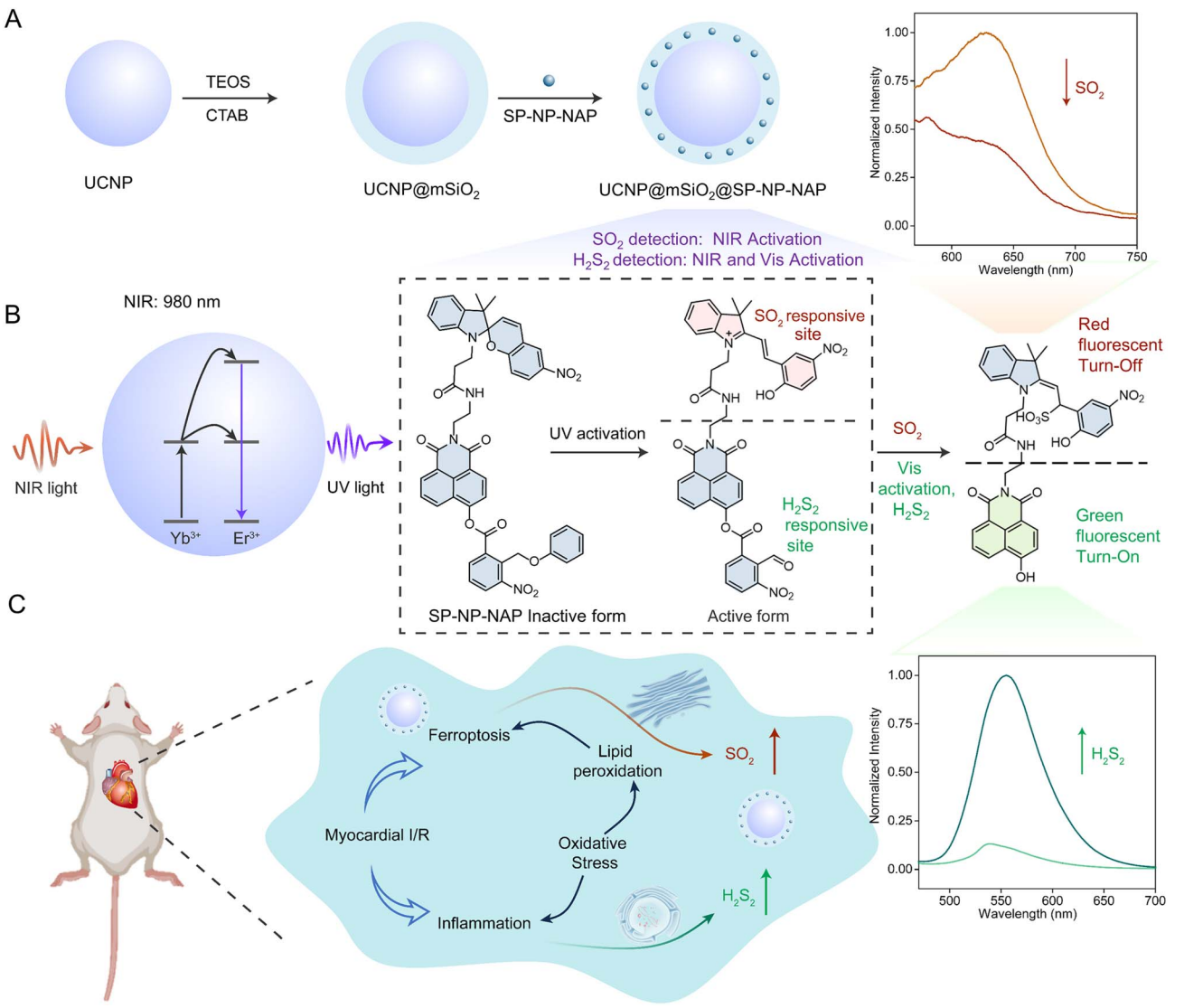

Scheme 1 Schematic representation of a light-activated nanoprobe for controllable monitoring of H_2S_2 and SO_2 in cardiac I/R injury. (A) The fabrication process of UCNP@mSiO$_2$@SP-NP-NAP. (B) Illustration of the response mechanism of NIR light-activated probe SP-NP-NAP to H_2S_2 and SO_2. NIR light activation under 980 nm for 30 min; visible light activation under 550 nm for 10 min; for SO_2 and H_2S_2 detection, the excitation wavelengths are 540 and 460 nm, respectively. (C) UCNP@mSiO$_2$@SP-NP-NAP for simultaneous detection of H_2S_2 and SO_2 in cardiac I/R injury accompanied by ferroptosis.

during ferroptosis processes *via* NIR-controlled switching of the responsiveness of the nanoprobe. *In situ* fluorescence imaging of endogenous H_2S_n and SO_2 could not only be used for the precise diagnosis of cardiac I/R damage but also revealed that cardiac I/R injury could be effectively attenuated by inhibiting the ferroptosis processes.

Results and discussion

Synthesis and characterization of SP-NP-NAP

Spiropyrans (SP) and 2-nitrobenzyl alcohol are widely used as representative photochromic dyes in photochemistry.[9,40] Upon exposure to UV light (365 nm), SP undergoes a reversible transformation into the merocyanine (MR) state that contains a specific C=C bond, which serves as the reaction site for SO_2. The 2-nitrophenyl group is also activated by UV light to yield an aldehyde product, which can act as the responsive site for H_2S_n through nucleophilic reaction.[41] To investigate the interaction between H_2S_n and SO_2, we have designed the photoactivated fluorescent probe (SP-NP-NAP) to simultaneously detect them. In this probe design, SP and naphthylamide were introduced as fluorescent moieties. The responsive sites were released upon light activation to simultaneously detect SO_2 and H_2S_n. The synthetic route of the SP-NP-NAP probe is displayed in the ESI (Fig. S1).† NMR and high-resolution mass spectrometry were used to validate the successful synthesis of SP-NP-NAP (Fig. S2–S14†).

We examined the spectral properties of SP-NP-NAP under UV/Vis light irradiation. The UV-Vis absorption and fluorescence spectra of the probe were measured. SP-NP-NAP exhibited a strong absorption peak at 360 nm, but no significant fluorescence signal was detected (Fig. S15A and S16A†). Under exposure to UV light at 365 nm, a new absorption signal emerged at 560 nm, while a fluorescence signal at 640 nm was observed excited at 540 nm. These observations are attributed to the transformation of SP to the MR structure within the probe following UV light activation. The closed spiro-ring state of SP restricts π-delocalization, while UV light activation prompts the reopening of the π-bridge to form the MR (opened spiro-ring). In this state, electron transfer between the donor and acceptor occurred, consequently releasing a fluorescent signal.[42]

To explore the reversibility of transition between SP and MR, we measured the fluorescence and absorption of SP-NP-NAP involving alternating exposure of the probe to UV light at 365 nm and Vis light at 550 nm. Fig. S15B and S16B† show that the reversible transformation between SP and MR structure could be easily realized through alternating UV/Vis light irradiation. Furthermore, we observed that repetitive illumination had minimal effect on the switching efficiency, indicating the structure change of SP-NP-NAP with good reversibility. We subsequently explored the probe's capability to monitor H_2S_2 and SO_2. Upon the addition of SO_2, the fluorescence signal at 640 nm was significantly diminished following UV light activation and then excited by 540 nm laser light (Fig. S17A†), demonstrating the feasibility of SO_2 monitoring. Considering the substantial overlap between the excitation wavelength (540 nm) of SP and the emission wavelength (550 nm) of naphthalimide, it led to the occurrence of fluorescence resonance energy transfer (FRET).[26] To avoid the FRET effect and achieve simultaneous detection of SO_2 and H_2S_2 at dual wavelengths, we exposed the probe under Vis light for 10 min. This illumination converted the MR into the SP structure. Subsequently, a strong fluorescent signal was observed at 550 nm under 460 nm light excitation in the presence of H_2S_2 after Vis light activation (Fig. S17B†). The results imply that the probe can be employed for the simultaneous detection of SO_2 and H_2S_2 based on the reversible SP/MR structure variation through UV/Vis light activation.

Preparation and characterization of the UCNP@mSiO$_2$@SP-NP-NAP nanoprobe

Compared to UV, NIR light has deep tissue penetration and less photodamage; therefore, we propose to use NIR light instead of UV light. Herein, we used a thermal decomposition method to synthesize the core–shell structure of UCNPs ($NaYF_4$:Yb/Tm@$NaYF_4$), which can convert NIR excitation into UV emission. As shown in Fig. S18,† the core–shell structured UCNP was characterized by X-ray diffraction (XRD), confirming the hexagonal crystalline phase of the nanoparticles. Moreover, the core–shell structured UCNPs were characterized by transmission electron microscopy (TEM). The TEM images showed well-defined hexagonal shapes with homogeneous particle sizes (approximately 30 nm in diameter), as illustrated in Fig. 1A and B. To realize the loading of SP-NP-NAP, we prepared UCNP@mSiO_2 by coating mesoporous SiO_2 onto the surface of UCNP. It could be observed that UCNP@mSiO_2 retained it monodisperse properties, exhibiting an approximate size of 70 nm (Fig. 1C). Subsequently, the light-responsive small molecule fluorescent probe, SP-NP-NAP, was loaded into UCNP@mSiO_2 to produce UCNP@mSiO_2@SP-NP-NAP, employing NIR-light simulated detection of SO_2 and H_2S_2. The hydrated particle size of the nanoprobe was approximately 114.8 nm (Fig. S19†), while the zeta potential was around −22.7 mV, indicating good dispersibility and stability (Fig. S20†). Fig. 1D illustrates the characterization of UCNP, UCNP@mSiO_2, and UCNP@mSiO_2@SP-NP-NAP using Fourier transform infrared spectroscopy (FTIR). Compared with UCNP, UCNP@mSiO_2 exhibited a distinctive Si–O band at 1060 cm^{-1} (Fig. 1D). Furthermore, the FTIR spectrum of UCNP@mSiO_2@SP-NP-NAP displayed characteristic absorbance peaks at 1660 (–CO–NH–) and 1545 ($–NO_2$) cm^{-1}, confirming the successful immobilization of SP-NP-NAP within UCNP@mSiO_2.

We then assessed the UCNP@mSiO_2@SP-NP-NAP nanoprobe under NIR irradiation. UCNP can convert NIR light to UV emission, which can change the structure from ring-closed to ring-opened SP. As shown in Fig. 1E, the ring-closed SP displayed a maximum absorption at approximately 360 nm, which overlapped with the emission peak of UCNPs within the UV region due to the $^3I_6 \rightarrow {}^3F_4$ and $^1D_2 \rightarrow {}^3H_6$ transitions of Tm^{3+} (Fig. S21†). Subsequently, the emission of UCNP@mSiO_2@SP-NP-NAP was studied under 980 nm excitation. Compared to UCNPs@mSiO_2, UCNP@mSiO_2@SP-NP-NAP showed a reduced

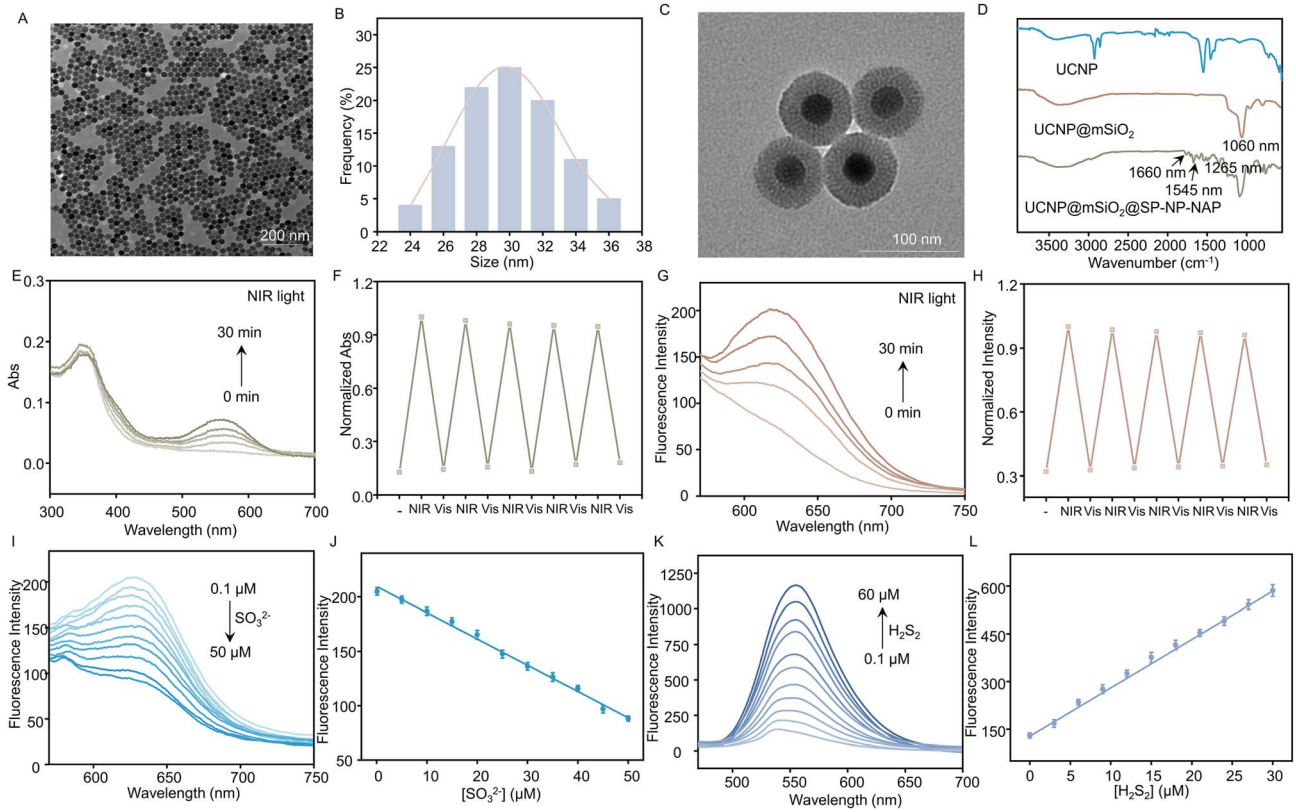

Fig. 1 Characterization of nanoprobe UCNP@mSiO$_2$@SP-NP-NAP. The TEM images of (A) UCNPs and (C) UCNP@mSiO$_2$. (B) Histogram of the size distribution of UCNPs. (D) FTIR spectra of UCNP, UCNP@mSiO$_2$, and UCNP@mSiO$_2$@SP-NP-NAP. The (E) absorption and (G) fluorescence spectra of UCNP@mSiO$_2$@SP-NP-NAP irradiation with NIR light (980 nm) in PBS (10 mM, pH 7.4). The photo-switching behaviors of UCNP@mSiO$_2$@SP-NP-NAP are based on the variations of (F) absorbance and (H) fluorescence signal in PBS (10 mM, pH 7.4). The fluorescence spectra and the linear relationship of light-activated nanoprobes for detection of (I and J) Na_2SO_3 (0.1–50 μM) and (K and L) H_2S_2 (0.1–60 μM). For fluorescence detection of Na_2SO_3/H_2S_2, the corresponding activation wavelengths were NIR/Vis, respectively.

emission at 360 nm (Fig. S21†). This indicated that SP-NP-NAP could effectively absorb the UV light emission from UCNPs@mSiO$_2$ to realize the NIR light-activated optical switching.

We investigated the response of the nanoprobe under alternating NIR (980 nm)/Vis (550 nm) light. A new absorption peak at 560 nm appeared with the extension of irradiation time and the signal remained stable after 30 min of NIR light illumination (Fig. 1E). Furthermore, the peak at 560 nm gradually decreased under Vis light irradiation, which was attributed to the interconversion of MR back to SP. The reversibility was also confirmed through five cycles of alternating NIR/Vis light illumination (Fig. 1F). It can be seen that the performance of the nanoprobe activated by NIR light is similar to that of the SP-NP-NAP probe under UV light illumination (Fig. S15 and S16†).

Detection of SO_2 and H_2S_2 *via* UCNP@mSiO$_2$@SP-NP-NAP

We evaluated the ability to detect SO_2 and H_2S_2 with UCNP@mSiO$_2$@SP-NP-NAP under alternating NIR/Vis light irradiation. Following activation by NIR light, the absorption intensity of the nanoprobe at 560 nm gradually decreased upon the addition of Na_2SO_3 (Fig. S22A†). This observation indicated that UCNP@mSiO$_2$@SP-NP-NAP could be employed to monitor the fluctuations of SO_2. Then, the nanoprobe was further activated by Vis light, and different concentrations of H_2S_2 were added. The absorption peak at 450 nm corresponding to naphthalimide gradually increased, while the absorption peak at 360 nm decreased (Fig. S22B†). Next, the fluorescence spectra of UCNP@mSiO$_2$@SP-NP-NAP were further investigated. In the absence of NIR irradiation, UCNP@mSiO$_2$@SP-NP-NAP was basically silent. However, the fluorescence signal at 640 nm was gradually enhanced with increasing NIR activation time (Fig. 1G), which was ascribed to the transition from the SP to MR structure. Similarly, we explored its reversibility by fluorescent spectroscopy. Under the alternating NIR/Vis light irradiation, the fluorescence intensity can be reversibly switched for at least 5 cycles (Fig. 1H).

UCNP@mSiO$_2$@SP-NP-NAP nanoprobe was then explored to detect SO_2 and H_2S_n. Here, we have chosen Na_2SO_3 and H_2S_2 as models for the study of SO_2 and H_2S_n, respectively. The nanoprobe was activated by NIR light for 30 min and then excited by 540 nm light. As shown in Fig. 1I, the fluorescence signal at 640 nm decreased rapidly after adding different concentrations of Na_2SO_3, indicating that the nanoprobe could be used to monitor the changes in SO_2 levels. Moreover, a good linear relationship was obtained with the concentration of

Na_2SO_3 over the range of 0.1–50 μM. The linear regression equation was $Y = 209.5868 - 2.4145[Na_2SO_3]$ (Fig. 1J), and the detection limit was calculated to be 0.24 μM based on $3\sigma/k$, where σ represents the standard deviation of the blank measurement, and k is the slope. We then examined the response of the nanoprobe to H_2S_2. After exposure to NIR light for 30 min, the UCNP@mSiO$_2$@SP-NP-NAP nanoprobe was further activated by Vis light exposure for 10 min. As shown in Fig. 1K, the fluorescence signal at 550 nm increased rapidly with increasing H_2S_2 concentration, indicating that the nanoprobe could be used for H_2S_2 detection. Similarly, a reliable linear relationship was established over the H_2S_2 concentration range of 0.1–30 μM. The linear regression equation was determined as $Y = 15.2065[H_2S_2] + 135.0270$ (Fig. 1L), and the detection limit was calculated to be 0.18 μM based on $3\sigma/k$. The results revealed the feasibility of detecting SO_2 and H_2S_2 through NIR/Vis light activation.

Once it was determined that the probe could monitor SO_2 and H_2S_2 separately, we investigated its potential for simultaneous detection of both analytes. We introduced various concentrations of Na_2SO_3 in the presence of H_2S_2. As shown in Fig. S23A,† the absorption intensity at 560 nm gradually decreased with the increase of Na_2SO_3 concentration, while the absorption peak at around 450 nm for naphthalimide remained unchanged. We then tested whether the presence of Na_2SO_3 would affect the detection of H_2S_2. As expected, the absorption peak at 450 nm gradually increased, while the peak at 560 nm for MR remained unaltered (Fig. S23B†). The fluorescence signal of the nanoprobe was further assessed in the presence of SO_2 and H_2S_2. As shown in Fig. S24A,† the fluorescence signal decreased rapidly as Na_2SO_3 concentration increased in the presence of H_2S_2, and the linear regression equation (Fig. S24B†) was determined as $Y = 207.3708 - 2.3806[Na_2SO_3]$. The linear relationship was consistent with that of in the absence of H_2S_2, indicating that H_2S_2 presence did not affect the detection of Na_2SO_3. Subsequently, we examined the fluorescence signal changes for H_2S_2 in the presence of Na_2SO_3 (Fig. S24C†), and the associated linear relationship equation was $Y = 15.6603[H_2S_2] + 127.9515$ (Fig. S24D†). Negligible changes were observed compared to that in the absence of Na_2SO_3, suggesting the presence of Na_2SO_3 did not affect the determination of H_2S_2. These results confirmed that UCNP@mSiO$_2$@SP-NP-NAP could be used to simultaneously detect SO_2 and H_2S_2 without cross-talk.

To assess the selectivity of the nanoprobe, a series of biological substances were measured, such as biothiols (Hcy, NAC, Cys, and GSH) reactive oxygen and reactive nitrogen species (H_2O_2, ClO^-, and $NaNO_2$), and various ions (Br^-, I^-, Cl^-, S^{2-}, CO_3^{2-}, Na^+, K^+), persulfides ($Na_2S_2O_4$, $Na_2S_2O_5$, CysSSCys and CH_3SSSCH_3), hydropersulfides (CysSSH and GSSH), and protein persulfides (papain and glyceraldehyde 3-phosphate dehydrogenase). Notably, these substances did not cause an obvious change in the fluorescent signal of UCNP@mSiO$_2$@SP-NP-NAP (Fig. S25 and S26†), indicating that the nanoprobe had good selectivity for SO_2 and H_2S_2 measurement. Furthermore, we investigated the time-dependent fluorescence signal of UCNP@mSiO$_2$@SP-NP-NAP to SO_2 and H_2S_2. As shown in Fig. S27,† the nanoprobe could respond to SO_2 within 5 min and H_2S_2 within 40 min, respectively. To employ the nanoprobe for the application of the biological system, we evaluated the effect of pH on the probe. As shown in Fig. S28,† the nanoprobe was not affected by pH over the range of 4–9. After adding SO_2 or H_2S_2, the nanoprobe with a robust fluorescence signal was observed under physiological conditions. These results further demonstrated the potential applications of UCNP@mSiO$_2$@SP-NP-NAP for detecting SO_2 and H_2S_2 in living organisms.

Detection of SO_2 and H_2S_2 in living cells *via* UCNP@mSiO$_2$@SP-NP-NAP

We investigated the nanoprobe in living cells under NIR/Vis light irradiation. Firstly, we tested the cytotoxicity of UCNP@mSiO$_2$@SP-NP-NAP in H9C2 (rat cardiomyoblast cell line) and HeLa (human cervical carcinoma cell line) cells. Cell Counting Kit-8 (CCK-8) experiments showed that UCNP@mSiO$_2$@SP-NP-NAP exhibited low cytotoxicity (Fig. S29†). We then investigated the feasibility of the nanoprobe for sensing analytes in living cells. The HeLa cells were imaged after co-incubation with UCNP@mSiO$_2$@SP-NP-NAP for 3 h, followed by irradiation with NIR/Vis light for nanoprobe activation, respectively. As shown in Fig. S30,† a minimal fluorescent signal was observed without NIR/Vis light irradiation. However, after activation with NIR light for 30 min and then excitation by 561 nm laser light, the red channel exhibited a clear fluorescence signal. The signal was attributed to the response of MR-NP-NA due to the NIR-triggered structural change of SP-NP-NAP (Scheme S1†). Subsequent irradiation with Vis light for 10 min caused the change of probe structure from MR to SP, and led to the disappearance of the red fluorescence signal (Fig. S30†). This phenomenon indicated that cell imaging using UCNP@mSiO$_2$@SP-NP-NAP could be effectively modulated through NIR/Vis light activation, providing the foundation for the detection of SO_2 and H_2S_2 in cells by regulation of the probe structure through light illumination. When the cells were alternatively irradiated with NIR light for 30 min, the fluorescent signal of the red channel, excited at 561 nm, was turned on and the intensity was well maintained (Fig. S30†). It further demonstrated the excellent reversibility of UCNP@mSiO$_2$@SP-NP-NAP.

We further investigated the performance of UCNP@mSiO$_2$@SP-NP-NAP for imaging intracellular SO_2 and H_2S_2 in living cells (Fig. 2). UCNP@mSiO$_2$@SP-NP-NAP was pre-incubated with cells before NIR light irradiation. As shown in Fig. 2A (control group), after a 30 min activation with NIR light, a bright fluorescence signal was observed in the red channel under 561 nm laser light excitation. Conversely, the green channel exhibited a minimal signal. After culturing with Na_2SO_3, the fluorescence signal in the red channel significantly decreased, while the green fluorescence signal remained sparse. As for H_2S_2 imaging, we observed a strong red fluorescence signal along with a weak green fluorescence signal. To avoid the FRET effect and enable the sensitive detection of H_2S_2 at 550 nm, we induced the structural transition from MR to SP through Vis light illumination. In the control group (Fig. 2A),

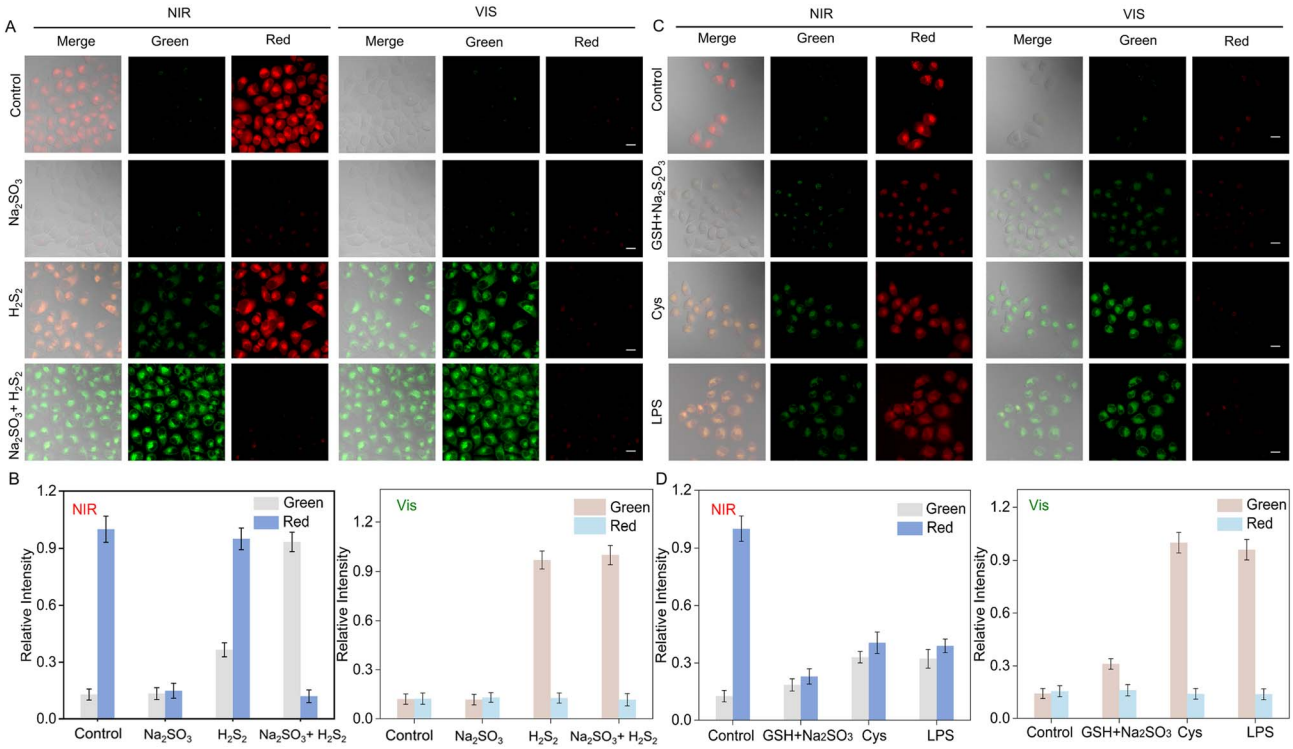

Fig. 2 Confocal laser scanning microscopy images of HeLa cells incubated with UCNP@mSiO$_2$@SP-NP-NAP. (A) The images of exogenous Na_2SO_3 (50 μM), H_2S_2 (50 μM), and Na_2SO_3 (50 μM) + H_2S_2 (50 μM), respectively. (B) The images of endogenous Na_2SO_3 and H_2S_2. Control group: without any treatments; GSH + $Na_2S_2O_3$ group: cells pretreated with $Na_2S_2O_3$ (200 μM) and GSH (500 μM) for 60 min; Cys group: cells pretreated with Cys (200 μM) for 60 min; LPS group: cells pretreated with LPS (1 μg mL^{-1}) for 12 h. (C) and (D) are relative fluorescence intensities in (A) and (B), respectively. NIR irradiation: 30 min; Vis irradiation: 10 min. Vis irradiation was performed following NIR irradiation. Red fluorescent channel: λ_{em} = 610–670 nm (λ_{ex} = 561 nm); green fluorescent channel: λ_{em} = 520–580 nm (λ_{ex} = 488 nm), scale bar: 20 μm. Error bars represent mean ± S.D. from three independent replicates.

following an additional 10 min activation with Vis light, the red fluorescence signal disappeared, which was ascribed to the structure shift from MR-NP-NA to SP-NP-NA. Na_2SO_3 could not trigger the fluorescent response from SP-NP-NA, resulting in no red fluorescence signal upon the exogenous addition of 50 μM Na_2SO_3. However, in the presence of exogenous H_2S_2, an enhancement of the green fluorescence signal was observed compared to the H_2S_2 group activated only by NIR light. This indicated that the nanoprobe could be effectively applied for sensitive detection of H_2S_2 in cells through NIR and Vis light modulation. We further investigated UCNP@mSiO$_2$@SP-NP-NAP for the simultaneous detection of SO_2 and H_2S_2. After NIR light activation, we observed a faint red signal and a significant green fluorescence in the presence of exogenous Na_2SO_3 (50 μM) and H_2S_2 (50 μM). For further Vis light activation, almost no red signal was observed. Subsequently, we tried to use the nanoprobe to quantitatively analyze Na_2SO_3 and H_2S_2 in living cells. As shown in Fig. S31,† we can obtain a relatively good linear relationship for Na_2SO_3 or H_2S. The results indicated that UCNP@mSiO$_2$@SP-NP-NAP could be applied for the simultaneous imaging of SO_2 and H_2S_2 by NIR/Vis light modulation.

We further evaluated the feasibility of the nanoprobe for imaging endogenous SO_2 and H_2S_2. Previous studies showed that $Na_2S_2O_3$ and GSH could be converted to Na_2SO_3 catalyzed by thiosulfate transsulfatase.[43] The cells were pretreated with $Na_2S_2O_3$ (200 μM) and GSH (500 μM) for 60 min. Then, the cells were exposed to NIR light for 30 min and excited using 561 nm laser light. Following NIR light activation, a significant decrease in the fluorescent signal could be observed in the red channel, as well as a weak change in green fluorescence. This indicated that the UCNP@mSiO$_2$@SP-NP-NAP could be applied to detect endogenous SO_2. It has been reported that SO_2 and H_2S_2 could be generated *via* metabolism of L-cysteine (L-Cys) *in vivo*.[44] Upon treatment with L-Cys (200 μM) for 60 min, followed by NIR light exposure for 30 min, we observed an increased green signal under 488 nm light excitation and a reduced red fluorescence signal under 561 nm light excitation. Furthermore, after an additional 10 min of irradiation with Vis light, the green fluorescence was significantly enhanced, while the red fluorescence became negligible. The results suggested that the nanoprobe could effectively enable the simultaneous detection of endogenous SO_2 and H_2S_2 in cells with NIR/Vis light activation. Lipopolysaccharide (LPS) can induce the overproduction of cystathionine gamma-lyase (CSE), which mediates the metabolism of L-Cys to produce SO_2 and H_2S_2.[45] The release of SO_2 and H_2S_2 induced by LPS was investigated by treating the cells with LPS (1 μg mL^{-1}) for 12 h before incubation with

UCNP@mSiO$_2$@SP-NP-NAP. Compared with the control group, there was an increase in fluorescence intensity in the green channel and a significant decrease in fluorescence signal in the red channel after NIR light activation. After Vis light irradiation, bright green fluorescence was observed and the red fluorescence almost disappeared. The results indicated that the imaging of endogenous SO_2 and H_2S_2 could be achieved by NIR/Vis light modulation.

Imaging of SO_2 and H_2S_2 in H9C2 cells during ferroptosis

Ferroptosis is an iron-dependent form of non-apoptotic cell death, which is mainly characterized by elevated levels of ferrous ions and accumulation of lipid peroxides.[5,46] Here, we examined the fluctuation of SO_2 and H_2S_2 levels during ferroptosis in myoblastic cells. Erastin, a classical ferroptosis activator, effectively inhibits cystine uptake through the cystine/glutamate antiporter system, which in turn leads to ferroptosis.[7,47] Thus, we employed erastin as an inducer of ferroptosis to monitor the changes in SO_2 and H_2S_2 levels in H9C2 cells. Fig. 3A shows the changes of fluorescence signals for erastin-induced ferroptosis in comparison to the control group. Upon NIR light activation, a decrease in red fluorescence and an increase green fluorescence signal were observed after the addition of erastin. Furthermore, the green fluorescence was increased and the red fluorescence was reduced after Vis light

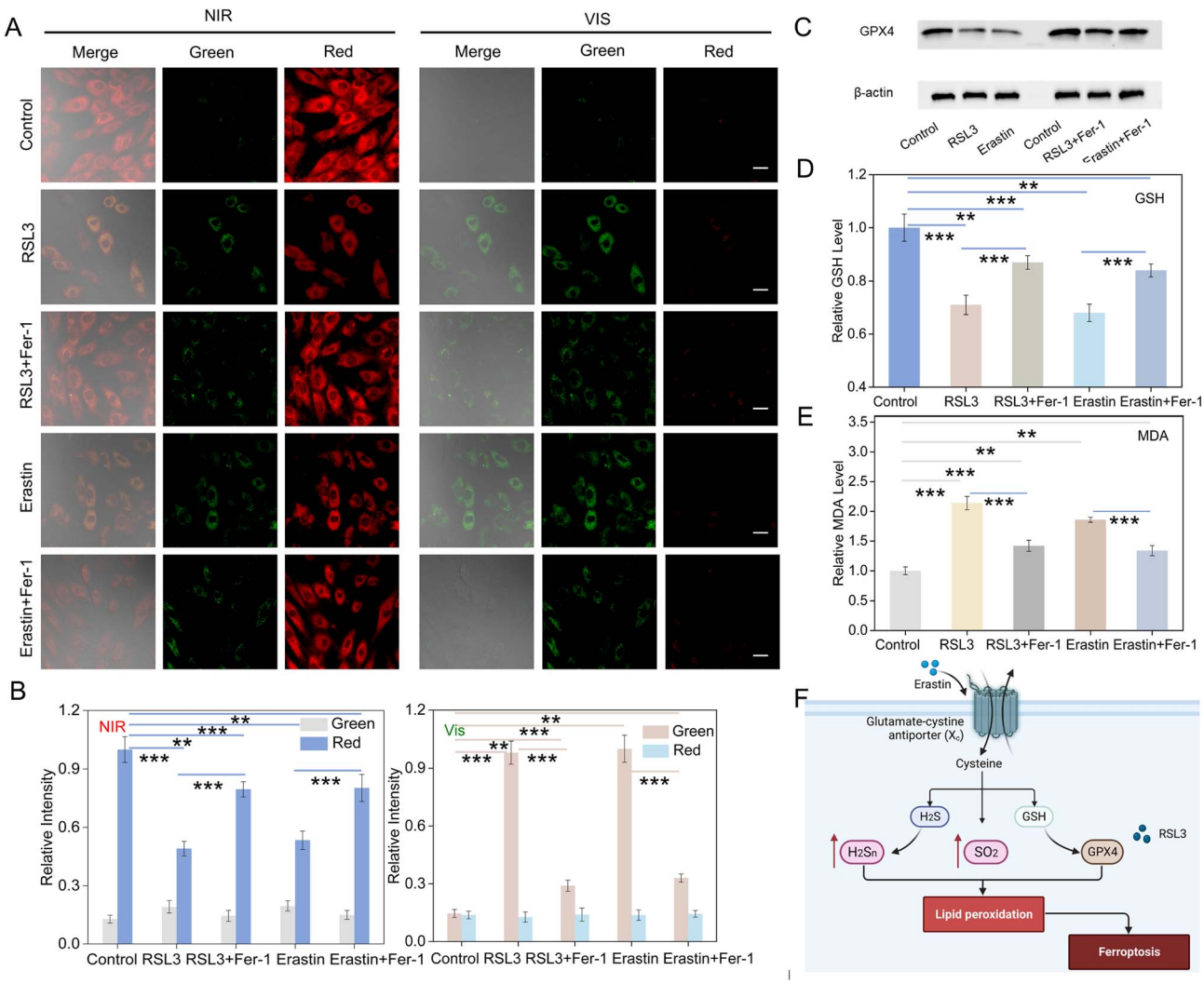

Fig. 3 Confocal laser scanning microscopy image of H9C2 cells cultured with UCNP@mSiO$_2$@SP-NP-NAP for erastin and RSL3-induced ferroptosis. (A) The imaging of variation of Na_2SO_3 and H_2S_2 levels during ferroptosis upon alternating NIR/Vis light activation. Control group: H9C2 cells cultured with UCNP@mSiO$_2$@SP-NP-NAP; RSL3 group: H9C2 cells pretreated with RSL3 (3 μM) for 6 h; RSL3 + Fer-1 group: cells co-incubated with RSL3 (3 μM) and Fer-1 (10 μM) for 6 h. Erastin group: cells pretreated with erastin (10 μM) for 2 h. Erastin + Fer-1 group: cells co-incubated with erastin (10 μM) and Fer-1 (10 μM) for 2 h. (B) Relative fluorescence intensity after NIR and Vis laser light activation in (A), respectively. (C) Western blotting analysis of GPX4 expression in different groups in (A). Relative contents of (D) GSH and (E) MDA in different groups as in (A). (F) Mechanism of erastin or RSL3-induced ferroptosis. NIR irradiation: 30 min; Vis irradiation: 10 min. Vis irradiation was performed after NIR irradiation. Red fluorescent channel: λ_{em} = 610–670 nm (λ_{ex} = 561 nm); green fluorescent channel: λ_{em} = 520–580 nm (λ_{ex} = 488 nm), scale bar: 20 μm. Error bars represent mean ± S.D. from three independent replicates. Statistical significance was calculated using one way ANOVA by Tukey's multiple comparisons test. *p < 0.05, **p < 0.01, and ***p < 0.001.

irradiation. Ferroinhibitor-1 (Fer-1) acts as an inhibitor of ferroptosis by inhibiting lipid peroxidation and regulating iron ion metabolism, thereby attenuating the ferroptosis process.[48,49] Interestingly, upon the introduction of the ferroptosis inhibitor Fer-1, the green fluorescence intensity decreased significantly, while the red channel fluorescence signal increased. The results indicated the simultaneous up-regulation of the concentrations of SO_2 and H_2S_2 during erastin-induced ferroptosis.

RSL3, another ferroptosis activator, was also applied to induce ferroptosis, which inhibited GPX4 and down-regulated the expression of GPX4 protein.[50,51] As shown in Fig. 3A, compared with the control group, an increase in green channel fluorescence signal and a decrease in red channel fluorescence signal were also observed after NIR light activation in response to RSL3 treatment. Moreover, the green fluorescence was enhanced while the red signal became negligible after Vis light irradiation. However, the treatment with Fer-1 and RSL3 only slightly enhanced the green fluorescent signal and attenuated the red fluorescent signal relative to the control group. All of this suggested that the RSL3-induced ferroptosis led to an up-regulation in the levels of SO_2 and H_2S_2. Furthermore, we investigated the levels of SO_2 and H_2S_2 in RSL3-treated cells at different incubation time. As shown in Fig. S32,† the fluorescence signal in the green channel was significantly enhanced, while the fluorescence signal in the red channel was gradually attenuated with the extension of incubation time. The data indicated that the nanoprobe could be employed to monitor the fluctuation of SO_2 and H_2S_2 in RSL3-induced cells. Although the nanoprobe was successfully applied to detect H_2S_2 and SO_2 in RSL3- and erastin-induced ferroptosis models, the verification of the occurrence of ferroptosis was also necessary. Therefore, western blotting analysis was further used to evaluate the process. It confirmed the significant reduction in GPX4 protein levels following stimulation with RSL3 or erastin, while the treatment with Fer-1 resulted in the upregulation of GPX4 expression. These results demonstrated the successful modeling of ferroptosis. Moreover, ferroptosis is characterized by the generation of lipid hydroperoxides (LPO), which impair cellular structure and integrity, serving as essential markers of ferroptosis.[52] Malondialdehyde (MDA), one of the main oxidation products of LPO, was employed to assess LPO levels in cells.[53] Furthermore, it also indirectly reflected the degree of tissue peroxidative damage.[54] In addition, the level of GSH could also serve as a vital indicator of the process of

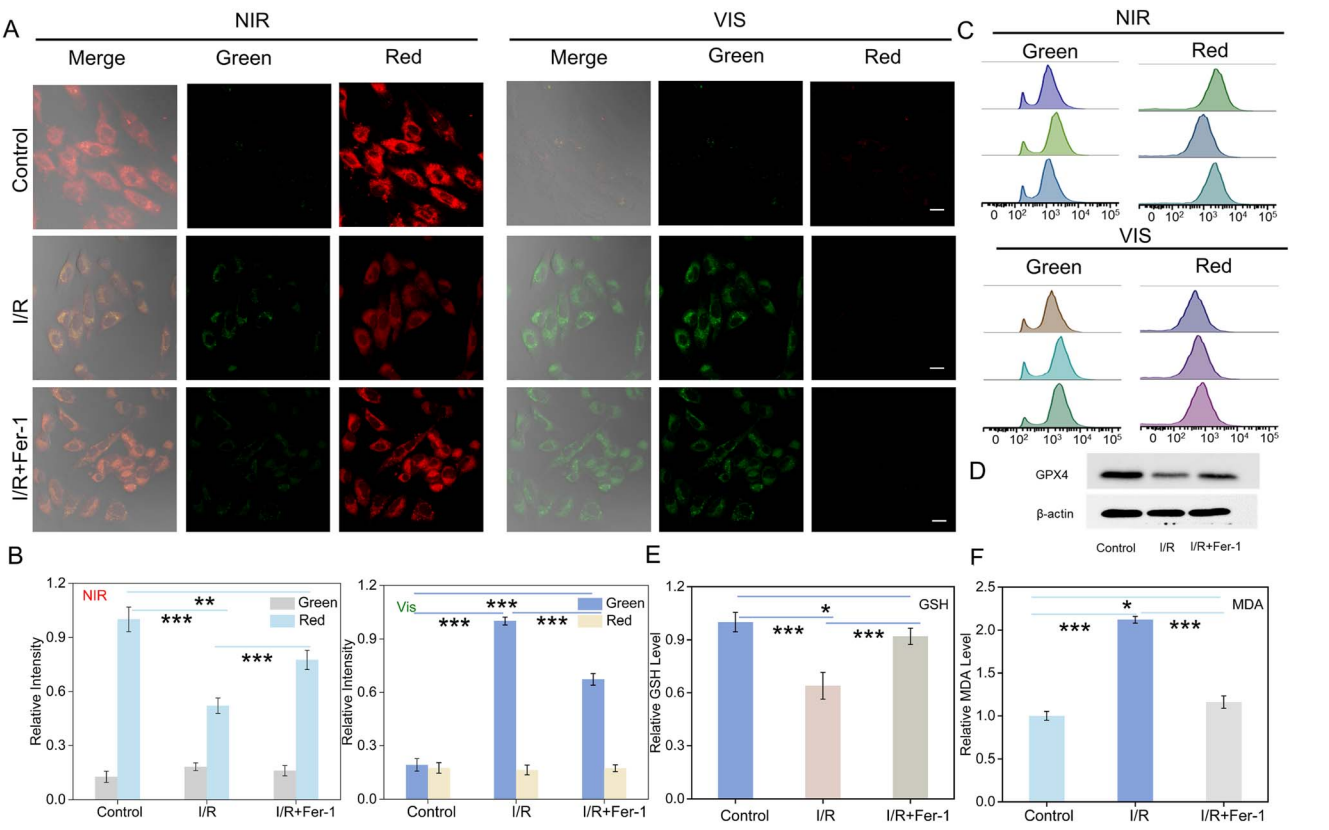

Fig. 4 Confocal laser scanning images of SO_2 and H_2S_2 in H9C2 cells during I/R injury. (A) Fluorescence imaging for H9C2 cells without treatment (control), I/R treated cells and I/R + Fer-1 treated cells. (B) Relative fluorescence intensity after NIR and Vis light activation as shown in (A). (C) The flow cytometry analysis for different groups of H9C2 cells as shown in (A). (D) Western blotting analysis of GPX4 expression for different groups of H9C2 cells as shown in (A). Relative levels of (E) GSH and (F) MDA for different groups of H9C2 cells as shown in (A). NIR light irradiation: 30 min; Vis light irradiation: 10 min. Vis irradiation was performed after NIR irradiation. Red fluorescent channel: $\lambda_{em} = 610–670$ nm ($\lambda_{ex} = 561$ nm); green fluorescent channel: $\lambda_{em} = 520–580$ nm ($\lambda_{ex} = 488$ nm), scale bar: 20 μm. Error bars represent mean ± S.D. from three independent replicates. Statistical significance was calculated using one way ANOVA by Tukey's multiple comparisons test. *$p < 0.05$, **$p < 0.01$, and ***$p < 0.001$.

ferroptosis.[55] Therefore, we detected the changes in the MDA and GSH levels (Fig. 3D and E) in erastin or RSL3-treated H9C2 cells. As shown in Fig. 3D and E, erastin or RSL3 treatment resulted in increased MDA and decreased GSH levels. All data suggested that UCNP@mSiO$_2$@SP-NP-NAP could be applied to assess the levels of SO_2 and H_2S_2 during the ferroptosis process in living cells.

Visualization of endogenous SO_2 and H_2S_2 in cardiac cells during I/R injury

I/R injury, an extremely complex pathophysiological process, is often accompanied by ferroptosis.[55] It is well known that I/R injury causes mitochondrial damage, and antioxidants can protect I/R-induced mitochondria from damage.[56–58] Therefore, we investigated the dynamics of SO_2 and H_2S_2 levels and their roles during I/R injury in H9C2 cells.[59,60] As shown in Fig. 4A, after activation with NIR light, the I/R injury group exhibited a significant reduction in red fluorescence as compared with the control group. Conversely, the green fluorescence signal was significantly increased. These results indicated that I/R injury could result in the upregulation of the levels of SO_2 and H_2S_2. Subsequently, upon exposure to Vis light, the fluorescence signal in the red channel decreased, accompanied by an enhancement in fluorescence intensity in the green channel. As for the Fer-1 group, the red fluorescence signal significantly recovered in comparison to the I/R injury group, while the green fluorescence was decreased. After Vis light irradiation, the green fluorescence signal slightly enhanced, and the red fluorescence signal increased (Fig. 4A). The changes in relative fluorescence intensity were also provided in Fig. 4B. These results further indicated that I/R injury was linked with the occurrence of ferroptosis. Inhibiting the onset of the ferroptosis process effectively attenuated I/R injury. Moreover, the flow cytometry analysis was employed to confirm it (Fig. 4C). The trends in fluorescence intensity were well consistent with those of confocal imaging. Western blotting assay showed that GPX4 expression was significantly inhibited in the I/R injury group, while the introduction of Fer-1 led to upregulation of GPX4 expression (Fig. 4D). The levels of MDA and GSH were also tested separately. The levels of MDA decreased in the Fer-1 group compared to the I/R injury group, while the levels of GSH increased (Fig. 4F and G). In addition, the cell viability of different groups was determined by CCK-8 assay. As shown in Fig. S33,† the cell viability was obviously decreased after cellular I/R injury, while it was recovered for the I/R + Fer-1 group. This indicated that the Fer-1 could effectively reduce cellular I/R damage by inhibiting ferroptosis. These results revealed that UCNP@mSiO$_2$@SP-NP-NAP could be a powerful tool to assess the ferroptosis process in the I/R injury.

Monitoring of SO_2 and H_2S_2 in mouse cardiac I/R injury tissue

After investigating the relationship between ferroptosis and I/R injury in cells, we established a mouse cardiac I/R model for further study. Hematoxylin and eosin (H&E) sections were employed to verify the successful establishment of the mouse cardiac I/R model. As shown in Fig. 5A, the myocardial tissue in the control group displayed a dense and orderly structure with intact myocardial fibers. In contrast, the I/R injury group displayed disorganized myocardial tissue with several broken myocardial fibers. Compared with the I/R injury group, the

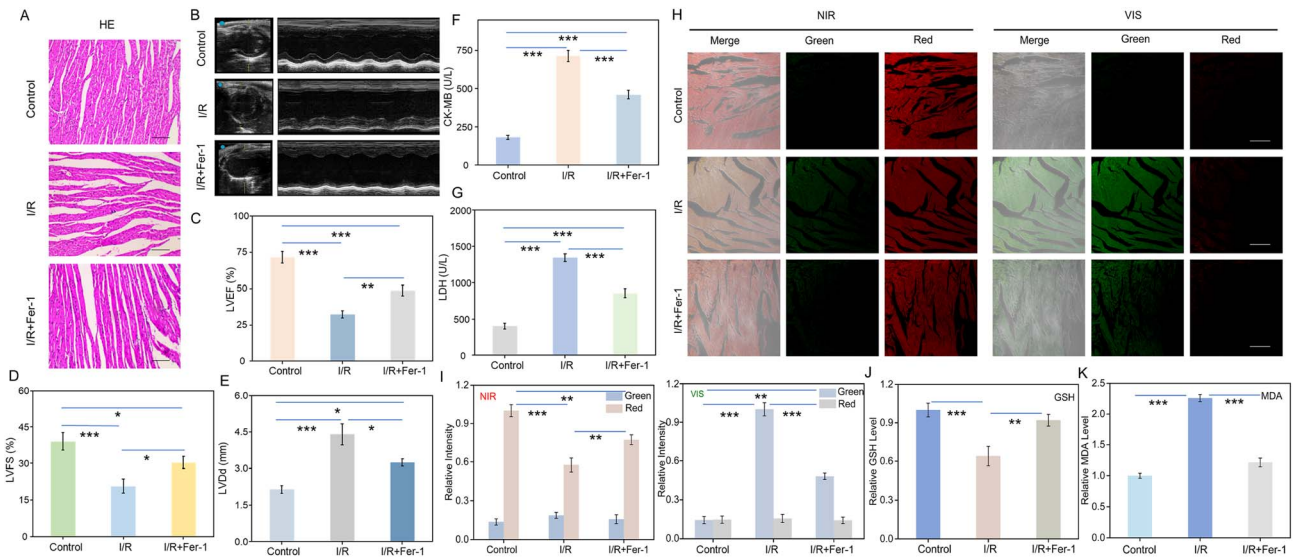

Fig. 5 Visual imaging of SO_2 and H_2S_2 in mouse cardiac I/R injury tissue. (A) H&E slices for control, I/R injury and I/R + Fer-1 group, respectively. (B) Representative m-mode echocardiographic images and cardiac functional parameters. Cardiac function was damaged *via* myocardial I/R as evidenced in increased (C) LVEF, (D) LVFS, and(E) LVDd. (F) CK-MB and (G) LDH levels in myocardial I/R and Fer-1 treatment. (H) Confocal images of control, I/R injury and I/R + Fer-1 treated mouse cardiac tissues. (I) Relative fluorescence intensity after activation with NIR and then Vis light as shown in (H). Relative content of (J) GSH and (K) MDA for control, I/R injury and I/R + Fer-1 group, respectively. NIR light irradiation: 30 min; Vis light irradiation: 10 min. Vis irradiation was performed after NIR irradiation. Red fluorescent channel: λ_{em} = 610–670 nm (λ_{ex} = 561 nm); green fluorescent channel: λ_{em} = 520–580 nm (λ_{ex} = 488 nm), scale bar: 200 μm. Error bars represent mean ± S.D. from three independent replicates. Statistical significance was calculated using one way ANOVA by Tukey's multiple comparisons test. *p < 0.05, **p < 0.01, and ***p < 0.001.

degree of myocardial tissue damage was significantly reduced in the Fer-1 treated group. As shown in Fig. 5B–E, noninvasive assessment of cardiac function after I/R injury was conducted using echocardiography, including the evaluation of left ventricular ejection fractions (LVEF), left ventricular fractional shortening (LVFS), and left ventricular end diastolic dimension (LVDd). The results revealed that Fer-1 is effective in mitigating impairment of myocardial function in the I/R group. In addition, creatine kinase-MB (CK-MB) and lactate dehydrogenase (LDH) are commonly used to evaluate cardiac function. As shown in Fig. 5F and G, levels of CK-MB and LDH exhibited significant elevation during I/R injury. However, Fer-1 reduced their expression levels. Subsequently, these tissues were imaged after incubated with UCNP@mSiO_2@SP-NP-NAP. Upon activation with NIR light, the I/R injury group demonstrated an enhancement of green signal accompanied by a reduction in red fluorescence compared to the control group (Fig. 5H). The green fluorescence signal was further enhanced, while the red fluorescence signal disappeared after further activation with Vis light irradiation. The results indicated that the levels of SO_2 and H_2S_2 were increased during I/R injury, further enhancing the antioxidant capacity of the myocardium during I/R injury.[61–65] Therefore, the upregulation of H_2S_n and SO_2 may be beneficial for alleviating I/R injury, and they show the potential to be biomarkers for diagnosing I/R injury. Conversely, compared to the I/R injury group, the Fer-1 treated group exhibited a decrease in the green fluorescence signal and a relative recovery of the red channel fluorescence signal (Fig. 5H). When Vis light was irradiated, the green fluorescence signal was much lower than that of the I/R injury group. Fig. 5J and K confirmed the increase of MDA and the decrease of the GSH level. These data suggested that the nanoprobe could be used to investigate the progression of ferroptosis during I/R injury. Inhibition of the ferroptosis process could reduce I/R damage and shows great potential for the treatment of cardiovascular disease.

Conclusions

We developed a NIR light-activated UCNP@mSiO_2@SP-NP-NAP nanoprobe for controllable measurement of the dynamics of SO_2 and H_2S_n levels. The introduction of UCNPs could turn on the dual reaction sites of SP-NP-NAP under NIR light illumination, leading to controllable simultaneous detection of SO_2 and H_2S_n with high sensitivity and selectivity. We successfully monitored intracellular SO_2 and H_2S_n through NIR/Vis light activation. Reversible alternation of NIR and Vis light could be achieved for at least 5 cycles. The results revealed that the levels of SO_2 and H_2S_n have been upregulated during the ferroptosis-related I/R injury process. They also showed that myocardial I/R injury could be effectively reduced by inhibiting the occurrence of ferroptosis, which indicated great potential for treating cardiovascular disease.

Data availability

Additional experimental data supporting this article are included in the ESI.† Reasonable requests for additional information can be made to the corresponding authors.

Author contributions

Xianzhu Luo: conceptualization, investigation, writing – original draft. Cuiling Zhang: supervision, conceptualization, writing – review & editing, funding acquisition. Chenyang Yue: validation, investigation. Yuelin Jiang: investigation, visualization. Fei Yang: investigation. Yuezhong Xian: conceptualization, supervision, writing – review & editing, funding acquisition.

Conflicts of interest

There are no conflicts to declare.

Acknowledgements

This research was supported by the National Natural Science Foundation of China (22274054, 21974050, 11727810), the Natural Science Foundation of Shanghai (20ZR1418000), and the Fundamental Research Funds for the Central Universities.

References

1 D. Ren, N. Quan, J. Fedorova, J. Zhang, Z. He and J. Li, *Redox Biol.*, 2020, **34**, 101556.
2 G. W. Reed, J. E. Rossi and C. P. Cannon, *Lancet*, 2017, **389**, 197–210.
3 Y. H. Hsieh, S. S. Huang, F. C. Wei and L. M. Hung, *Circ. J.*, 2007, **71**, 423–428.
4 A. W. Rookyard, J. Paulech, S. Thyssen, K. A. Liddy, M. Puckeridge, D. K. Li, M. Y. White and S. J. Cordwell, *Antioxid. Redox Signaling*, 2021, **34**, 11–31.
5 S. J. Dixon, K. M. Lemberg, M. R. Lamprecht, R. Skouta, E. M. Zaitsev, C. E. Gleason, D. N. Patel, A. J. Bauer, A. M. Cantley, W. S. Yang, B. I. Morrison and B. R. Stockwell, *Cell*, 2012, **149**, 1060–1072.
6 Y. Xie, W. Hou, X. Song, Y. Yu, J. Huang, X. Sun, R. Kang and D. Tang, *Cell Death Differ.*, 2016, **23**, 369–379.
7 B. R. Stockwell, J. P. Friedmann Angeli, H. Bayir, A. I. Bush, M. Conrad, S. J. Dixon, S. Fulda, S. Gascón, S. K. Hatzios, V. E. Kagan, K. Noel, X. Jiang, A. Linkermann, M. E. Murphy, M. Overholtzer, A. Oyagi, G. C. Pagnussat, J. Park, Q. Ran, C. S. Rosenfeld, K. Salnikow, D. Tang, F. M. Torti, S. V. Torti, S. Toyokuni, K. A. Woerpel and D. D. Zhang, *Cell*, 2017, **171**, 273–285.
8 P. Xie, J. Liu, X. Yang, W. Zhu and Y. Ye, *Sens. Actuators, B*, 2022, **365**, 131937.
9 U. Barayeu, D. Schilling, M. Eid, T. N. Xavier da Silva, L. Schlicker, N. Mitreska, C. Zapp, F. Gräter, A. K. Miller, R. Kappl, A. Schulze, J. P. Friedmann Angeli and T. P. Dick, *Nat. Chem. Biol.*, 2023, **19**, 28–37.
10 A. Bindoli, J. M. Fukuto and H. J. Forman, *Antioxid. Redox Signaling*, 2008, **10**, 1549–1564.
11 K. Ono, T. Akaike, T. Sawa, Y. Kumagai, D. A. Wink, D. J. Tantillo, A. J. Hobbs, P. Nagy, M. Xian, J. Lin and J. M. Fukuto, *Free Radical Biol. Med.*, 2014, **77**, 82–94.

12 H. Kimura, *Antioxid. Redox Signaling*, 2015, **22**, 362–376.
13 H. Dong, Q. Zhou, L. Zhang and Y. Tian, *Angew. Chem., Int. Ed.*, 2019, **58**, 13948–13953.
14 V. S. Khodade, B. M. Pharoah, N. Paolocci and J. P. Toscano, *J. Am. Chem. Soc.*, 2020, **142**, 4309–4316.
15 V. S. Khodade, S. C. Aggarwal, B. M. Pharoah, N. Paolocci and J. P. Toscano, *Chem. Sci.*, 2021, **12**, 8252–8259.
16 B. M. Pharoah, C. Zhang, V. S. Khodade, G. Keceli, C. McGinity, N. Paolocci and J. P. Toscano, *Redox Biol.*, 2023, **60**, 102625.
17 B. M. Pharoah, V. S. Khodade, A. Eremiev, E. Bao, T. Liu, B. O'Rourke, N. Paolocci and J. P. Toscano, *Antioxidants*, 2022, **11**, 1010.
18 M. R. Jackson, S. L. Melideo and M. S. Jorns, *Biochemistry*, 2012, **51**, 6804–6815.
19 Y. Liu, K. Li, K. Xie, L. Li, K. Yu, X. Wang and X. Yu, *Chem. Commun.*, 2016, **52**, 3430–3433.
20 Y. Huang, H. Zhang, B. Lv, C. Tang, J. Du and H. Jin, *Antioxid. Redox Signaling*, 2022, **36**, 256–274.
21 Z. Meng, Z. Yang, J. Li and Q. Zhang, *Chemosphere*, 2012, **89**, 579–584.
22 J. Tang, M. A. Robichaux, K. Wu, J. Pei, N. T. Nguyen, Y. Zhou, T. G. Wensel and H. Xiao, *J. Am. Chem. Soc.*, 2019, **141**, 14699–14706.
23 X. Chen, W. Feng, H. Bisoyi, S. Zhang, X. Chen, H. Yang and Q. Li, *Nat. Commun.*, 2022, **13**, 3216.
24 E. A. Jares-Erijman and T. M. Jovin, *Nat. Biotechnol.*, 2003, **21**, 1387–1395.
25 J. Zhang, Y. Fu, H. H. Han, Y. Zang, J. Li, X. P. He, B. L. Feringa and H. Tian, *Nat. Commun.*, 2017, **8**, 987.
26 W. Zhang, F. Huo, Y. Yue, Y. Zhang, J. Chao, F. Cheng and C. Yin, *J. Am. Chem. Soc.*, 2020, **142**, 3262–3268.
27 J. M. Goldberg, F. Wang, C. D. Sessler, N. W. Vogler, D. Y. Zhang, W. H. Loucks, T. Tzounopoulos and S. Lippard, *J. Am. Chem. Soc.*, 2018, **140**, 2020–2023.
28 L. L. Wang, B. X. Chen, P. P. Peng, W. B. Hu, Z. P. Liu, X. H. Pei, W. H. Zhao, C. W. Zhang, L. Li and W. Huang, *Chin. Chem. Lett.*, 2017, **28**, 1965–1968.
29 E. A. Halabi and R. Weissleder, *J. Am. Chem. Soc.*, 2023, **145**, 8455–8463.
30 Y. X. Fu, X. Zhang, F. Cao, W. H. Wang, G. R. Qian and J. J. Zhang, *Sci. China: Chem.*, 2019, **62**, 1204–1212.
31 E. A. Halabi, Z. Thiel, N. Trapp, D. Pinotsi and P. Rivera-Fuentes, *J. Am. Chem. Soc.*, 2017, **139**, 13200–13207.
32 S. Yang, J. Jiang, A. Zhou, Y. Zhou, W. Ye, D. Cao and R. Yang, *Anal. Chem.*, 2020, **92**, 7194–7199.
33 M. Ye, Y. Kong, C. Zhang, Y. Lv, S. Cheng, D. Hou and Y. Xian, *ACS Nano*, 2021, **15**, 14253–14262.
34 M. Li, J. Zhao, H. Chu, Y. Mi, Z. Zhou, Z. Di, M. Zhao and L. Li, *Adv. Mater.*, 2019, **31**, 1804745.
35 X. Luo, Z. Cheng, R. Wang and F. Yu, *Anal. Chem.*, 2021, **93**, 2490–2499.
36 C. J. Carling, J. C. Boyer and N. R. Branda, *J. Am. Chem. Soc.*, 2009, **131**, 10838–10839.
37 Z. Chen, L. Zhou, W. Bing, Z. Zhang, Z. Li, J. Ren and X. Qu, *J. Am. Chem. Soc.*, 2014, **136**, 7498–7504.
38 Y. K. Yue, F. J. Huo, F. Q. Cheng, X. J. Zhu, T. Mafireyi, R. M. Strongin and C. X. Yin, *Chem. Soc. Rev.*, 2019, **48**, 4155–4177.
39 Y.-L. Qi, H. R. Wang, Q. J. Kang, L.-L. Chen, P. F. Qi, Z. X. He, Y.-S. Yang and H.-L. Zhu, *Sens. Actuators, B*, 2022, **352**, 130989.
40 W. Yuan, L. Sun, H. Tang, Y. Wen, G. Jiang, W. Huang, L. Jiang, Y. Song, H. Tian and D. Zhu, *Adv. Mater.*, 2005, **17**, 156–160.
41 L. Han, R. Shi, C. Xin, Q. Ci, J. Ge, J. Liu, Q. Wu, C. Zhang, L. Li and W. Huang, *ACS Sens.*, 2018, **3**, 1622–1626.
42 Z. Tian and A. Li, *Acc. Chem. Res.*, 2013, **46**, 269–279.
43 X. Zhang, L. Zhang, S. Liu, X. Zhu, P. Zhou, X. Cheng, R. Zhang, L. Zhang and L. Chen, *J. Hazard. Mater.*, 2022, **423**, 127179.
44 B. Yang, J. Xu and H. L. Zhu, *Free Radical Biol. Med.*, 2019, **145**, 42–60.
45 X. Y. Zhu, S. J. Liu, Y. J. Liu, S. Wang and X. Ni, *Cell. Mol. Life Sci.*, 2010, **67**, 1119–1132.
46 W. S. Yang and B. R. Stockwell, *Trends Cell Biol.*, 2016, **26**, 165–176.
47 W. S. Yang and B. R. Stockwell, *Chem. Biol.*, 2008, **15**, 234–245.
48 H. Yuan, Z. Han, Y. Chen, F. Qi, H. Fang, Z. Guo, S. Zhang and W. He, *Angew. Chem., Int. Ed.*, 2021, **60**, 8174–8181.
49 G. Miotto, M. Rossetto, M. L. Di Paolo, L. Orian, R. Venerando, A. Roveri, A. M. Vučković, V. Bosello Travain, M. Zaccarin, L. Zennaro, M. Maiorino, S. Toppo, F. Ursini and G. Cozza, *Redox Biol.*, 2020, **28**, 101328.
50 R. Lin, Z. Zhang, L. Chen, Y. Zhou, P. Zou, C. Feng, L. Wang and G. Liang, *Cancer Lett.*, 2016, **381**, 165–175.
51 L. Chen, W. S. Hambright, R. Na and Q. Ran, *J. Biol. Chem.*, 2015, **290**, 28097–28106.
52 T. Liu, W. Liu, M. Zhang, W. Yu, F. Gao, C. Li, S. B. Wang, J. Feng and X. Z. Zhang, *ACS Nano*, 2018, **12**, 12181–12192.
53 J. You, F. Yuan, S. Cheng, Q. Kong, Y. Jiang, X. Luo, Y. Xian and C. Zhang, *Chem. Mater.*, 2022, **34**(15), 7078–7089.
54 H. Chen, W. Tian and K. Huang, *Toxicol. Lett.*, 2013, **216**, 181–188.
55 T. Liang, T. Qiang, L. Ren, F. Cheng, B. Wang, M. Li, W. Hu and T. D. James, *Chem. Sci.*, 2022, **13**, 2992–3001.
56 E. R. Dabkowski, C. L. Williamson and J. M. Hollander, *Free Radical Biol. Med.*, 2008, **45**, 855–865.
57 J. Wang, S. Toan and H. Zhou, *Angiogenesis*, 2020, **23**, 299–314.
58 F. Arslan, D. P. de Kleijn and G. Pasterkamp, *Nat. Rev. Cardiol.*, 2011, **8**, 292–300.
59 L. Yang, Y. Ren, W. Pan, Z. Yu, L. Tong, N. Li and B. Tang, *Anal. Chem.*, 2016, **88**, 11886–11891.
60 E. T. Chouchani, V. R. Pell, E. Gaude, D. Aksentijevic, S. Y. Sundier, E. L. Robb, A. Logan, S. M. Nadtochiy, E. N. J. Ord, A. C. Smith, F. Eyassu, R. Shirley, C. H. Hu, A. J. Dare, A. M. James, S. Rogatti, R. C. Hartley, S. Eaton, A. S. H. Costa, P. S. Brookes, S. M. Davidson, M. R. Duchen, K. Saeb-Parsy, M. J. Shattock, A. J. Robinson, L. M. Work, C. Frezza, T. Krieg and M. P. Murphy, *Nature*, 2014, **515**, 431–435.

61 S. Nandi, S. Ravindran and G. A. Kurian, *Biomed. Pharmacother.*, 2018, **97**, 271–279.
62 Y. Zhou, Z. Gu, C. Liu, S. Yang, X. Ma, Q. Chen, Y. Lei, K. Quan, J. Liu, Z. Qing and R. Yang, *Angew. Chem., Int. Ed.*, 2022, **61**, e202114504.
63 H. Kimura, *Antioxid. Redox Signaling*, 2015, **22**, 362–376.
64 H. Jin, Y. Wang, X. Wang, Y. Sun, C. Tang and J. Du, *Nitric Oxide*, 2013, **32**, 56–61.
65 Y. Huang, H. Zhang, B. Lv, C. Tang, J. Du and H. Jin, *Sci. Bull.*, 2021, **66**, 1604–1607.